Journal of
Applied
Crystallography
ISSN 0021-8898

Received 6 September 2004
Accepted 29 November 2004

X-ray absorption, refraction and resonant scattering tensors in selenated protein crystals: implications for data collection strategies in macromolecular crystallography

G. Bricogne,[a] S. C. Capelli,[b] G. Evans,[c,a] A. Mitschler,[d] P. Pattison,[e,g] P. Roversi[f,a] and M. Schiltz[g,a]*‡

[a]Global Phasing Ltd, Sheraton House, Castle Park, Cambridge CB3 0AX, UK, [b]ESRF, 6 rue Jules Horowitz, BP 220, F-38043 Grenoble cedex 9, France, [c]DIAMOND Project, CCLRC Rutherford Appleton Laboratory, Chilton, Didcot OX11 0QX, UK, [d]Institut de Génétique et de Biologie Moléculaire et Cellulaire, 1 rue Laurent Fries, B.P. 10142, F-67404 Illkirch cedex, France, [e]SNBL–ESRF, 6 rue Jules Horowitz, BP 220, F-38043 Grenoble cedex 9, France, [f]Laboratory of Molecular Biophysics, Department of Biochemistry, University of Oxford, South Parks Road, Oxford OX1 3QU, UK, and [g]École Polytechnique Fédérale de Lausanne (EPFL), Laboratoire de Cristallographie, CH-1015 Lausanne, Switzerland. Correspondence e-mail: marc.schiltz@epfl.ch

Polarized fluorescence spectra were recorded in the vicinity of the Se and Br K edges on crystals of the selenated protein aldose reductase in complex with a brominated inhibitor molecule. The X-ray absorption, refraction and resonant scattering tensors as a function of X-ray energy were derived from these data. Substantial dichroism and anisotropy of resonant scattering were observed in these crystals. It is predicted that these effects are present in many resonant scattering experiments in macromolecular crystallography and are likely to affect the diffraction data. As a consequence, the anomalous phasing signal in single- or multi-wavelength anomalous diffraction experiments can be optimized simply by choosing a judicious orientation of the crystal with respect to the polarization direction of the incident X-ray beam. A simple procedure is presented to achieve this, prior to any knowledge about the selenium sites.

© 2005 International Union of Crystallography
Printed in Great Britain – all rights reserved

1. Introduction

Experimental phasing methods which exploit the resonant (anomalous) scattering properties of specific atoms have known a tremendous success in macromolecular crystallography over the past two decades (Hendrickson, 1999). One of the most powerful of these methods, the MAD (multiple-wavelength anomalous diffraction) technique (Hendrickson, 1991), exploits the wavelength-dependence of the resonant scattering factors f' and f'' when the energy of the incident X-ray beam is in the vicinity of one of the absorption edges of the atoms in the crystal. The modulation of the scattering factors of a small subset of atoms by a variation of the wavelength of the incident X-ray beam is the basis for the solution of the phase problem by the MAD method. The element selenium plays a major role as anomalous scatterer in the application of the MAD method for the determination of protein structures since it can be used to replace sulfur in methionine residues by recombinant DNA technology (Hendrickson *et al.*, 1990) and because the Se K edge is located at a wavelength of λ = 0.9795 Å, which is readily accessible on most synchrotron sources.

Atomic resonant scattering occurs through electronic transitions from core levels to energy states within or just above the valence shell. Atomic resonant scattering terms for the isolated atom are spherically symmetrical. Chemical bonding can lower the symmetry, and make atomic resonant scattering terms anisotropic. Provided that the orientation of the atom and its bonding environment relative to the polarization of the beam is well defined over the time course of the measurement (as is the case for atoms in a crystal diffracting in an X-ray beam) this anisotropy gives rise to measurable resonant scattering anisotropy. Indeed, the anisotropy of anomalous scattering (AAS) has been evidenced experimentally in numerous investigations on salt and small-molecule crystals (Templeton & Templeton, 1980, 1982, 1985*a*,*b*, 1986, 1987, 1988, 1989, 1992, 1995, 1997; Petcov *et al.*, 1990; Kirfel *et al.*, 1991; Kirfel & Petcov, 1992; Kirfel & Morgenroth, 1993; Lippmann *et al.*, 1998). Most of these studies were interpreted in the framework of simple optical models, and for the explanation of most experimental observations a dipole approximation is sufficient (Dmitrienko, 1983, 1984; Kirfel *et al.*, 1991; Ovchinnikova & Dmitrienko, 2000). This allows a simple description of the AAS properties of an atom in terms of second-rank tensors. This approach (optical model and dipole approximation) will also be adopted in the present

‡ All authors contributed significantly to this work and are therefore listed in alphabetical order.

study. The effects of AAS are revealed by the changes in the diffracted intensities that occur upon changing the orientation of the crystal with respect to the direction of polarization of the incident X-ray beam. Also, in the presence of AAS, the polarization of the incident beam breaks the crystal symmetry. Since symmetry-related resonant scattering sites might experience the incident electric field under different polarization orientations, they are not necessarily equivalent anymore, as far as their scattering amplitudes are concerned. The vast majority of experimental studies have thus focused on the observation of screw-axis and glide-plane forbidden reflections, although it should be stressed that AAS affects all reflections, whether they are forbidden or non-forbidden. All experimental studies to date have shown that AAS is limited to a narrow spectral region in the immediate vicinity of the absorption edge.

Resonant diffraction and polarized resonant scattering are techniques that are currently at the forefront of experimental X-ray science in condensed matter studies (Hodeau *et al.*, 2001), in particular to investigate the orbital degree of freedom of electrons in oxides (Ishihara & Maekawa, 2002).

Since AAS is a local (or microscopic) effect, it is a function of the local site symmetry of the resonant atoms. The global (macroscopic) consequences of AAS are linear dichroism and birefringence which follow the point-group symmetry of the crystal. Dichroism manifests itself as an anisotropy of absorption, whereas birefringence is due to anisotropy of the speed of propagation (phase velocity) of X-rays. The relation between these microscopic and macroscopic optical properties is given by the so-called optical theorem (James, 1969) which relates the complex index of refraction n to the normal (Thomson) scattering factors at zero scattering angle (forward scattering) $f^0(0)$ and the resonant scattering factors f' and f'' of all atoms in the sample as a function of the photon energy of the incident radiation E

$$\begin{aligned} n(E) &= 1 - \alpha(E) - i\beta(E) \\ &= 1 - \frac{h^2c^2r_0}{2\pi E^2} \sum_j^{\text{elements}} \rho_j\big[f_j^0(0) + f_j'(E) + if_j''(E)\big], \end{aligned} \quad (1)$$

where r_0 is the classical electron radius, ρ_j is the number density of atoms of type j in the sample, and the other symbols have their usual meanings. The imaginary part of the index of refraction β is related to the linear absorption coefficient μ by

$$\mu(E) = \frac{4\pi E}{hc}\beta(E) = \frac{2hcr_0}{E} \sum_j^{\text{elements}} \rho_j f_j''(E). \quad (2)$$

In macromolecular crystallography, this relation is exploited to obtain near-edge values for the resonant scattering factor f'' from experimental absorption or fluorescence spectra.

Strictly speaking, equations (1) and (2) are valid only for a collection of isolated atoms, or for a sample for which spherical averaging is appropriate (*e.g.* liquids or powders). The extension of the optical theorem to the case of a single crystal with $N_{\rm uc}$ atoms in the unit cell is straightforward, assuming that the index of refraction and the resonant scattering factors are now written in tensorial form[1]

$$\begin{aligned} \mathbf{n}(E) &= 1 - \boldsymbol{\alpha}(E) - i\boldsymbol{\beta}(E) \\ &= 1 - \frac{h^2c^2r_0}{2\pi VE^2} \sum_j^{N_{\rm uc}} Q_j\big[f_j^0(0) + \mathbf{f}_j'(E) + i\mathbf{f}_j''(E)\big], \end{aligned} \quad (3)$$

where V is the volume of the unit cell and Q_j is the occupancy of atom j.

(Linear) birefringence is associated with the anisotropy of the real part of the index of refraction and is thus directly related to the $\mathbf{f}_j'$ scattering tensors:

$$1 - \boldsymbol{\alpha}(E) = 1 - \frac{h^2c^2r_0}{2\pi VE^2} \sum_j^{N_{\rm uc}} Q_j\big[f_j^0(0) + \mathbf{f}_j'(E)\big]. \quad (4)$$

(Linear) dichroism is associated with the anisotropy of the absorption tensor $\boldsymbol{\mu}$ and is thus directly related to the $\mathbf{f}_j''$ scattering tensors:

$$\boldsymbol{\mu}(E) = \frac{4\pi E}{hc}\boldsymbol{\beta}(E) = \frac{2hcr_0}{VE} \sum_j^{N_{\rm uc}} Q_j \mathbf{f}_j''(E). \quad (5)$$

Polarized absorption or fluorescence spectra can thus yield information about the resonant scattering tensors $\mathbf{f}_j''$, although there are some limitations to this method. Since birefringence and dichroism follow the point-group symmetry of the crystal, there can be no dichroism in cubic crystals (except for quadrupolar or higher-order effects), even in cases where there is significant AAS. The cubic point-group symmetry simply ensures that the summation over all sites in equation (5) always yield a scalar absorption coefficient. However, in crystals of lower symmetry there is a fair chance to observe dichroism and to infer information about AAS from such measurements.

Templeton & Templeton (1988) have shown that in selenolanthionine, a compound in which Se is covalently bonded to two sp^3 carbon atoms, as in selenomethionine, the f' and f'' factors vary respectively between −14.7 and −8.8 and between 0.8 and 7.7, depending on the orientation of the crystal with respect to the direction of polarization of the incident beam. These results were obtained from both polarized fluorescence spectra and from the direct measurement of AAS effects on the intensities of diffracted beams. Such variations are very substantial, similar to those obtained in a MAD experiment by changing the wavelength of the incident beam. Dichroism measurements on a selenated protein crystal were first reported by Hendrickson *et al.* (1989) and Fanchon & Hendrickson (1990). On crystals of selenobiotinyl Streptavidin, the authors observed marked variations (up to ∼5 eV) of the edge position as defined by the energy of minimal f' as well as variations of up to ∼1.5 for the maximum value of f'' at

[1] Tensors are denoted in bold type letters. Since the discussion takes place within the framework of the dipole approximation, only second-rank tensors occur and these are represented by 3 × 3 matrices. Addition of a scalar to a tensor [as *e.g.* in $f_j^0(0) + \mathbf{f}_j'(E)$] implicitly means that the scalar quantity is added to all diagonal elements of the matrix representing the tensor. Similarly, in tensorial expressions, the symbol 1 stands for the 3 × 3 identity matrix.

the white-line feature. In this crystal, all C—Se—C planes are nearly perpendicular (within 30°) to one of the crystal axes. A direct analysis of AAS from intensity measurements at different crystal orientations has also been reported by Fanchon & Hendrickson (1990). Despite clear evidence of AAS, the observed variations in f' and f'' factors are much smaller than those reported by Templeton & Templeton (1988) for crystals of selenolanthionine. A detailed analysis conducted by Fanchon & Hendrickson (1990) ascribed the smaller size of these differences to the larger energy spreads of the incident beam used in their experiments. Indeed, the spectral purity of the incident X-ray beam is a critical quantity since a poor energy resolution can completely smear out the effects of AAS. The experiments of Hendrickson *et al.* (1989) and Fanchon & Hendrickson (1990) were carried out on two different beamlines displaying estimated energy bandpasses of respectively ~4 and ~10 eV. In contrast, the measurements reported by Templeton & Templeton (1988) were conducted with a Si(220) monochromator, offering an energy resolution better than 2 eV. Polarized fluorescence measurements were also reported on crystals of selenomethionyl thioredoxin, but only marginal dichroism was observed (Hendrickson *et al.*, 1990).

With the advent of third-generation synchrotrons, X-ray beams of greater spectral purity are delivered more routinely and many experimentalists have made anecdotal observations of dichroism in selenated protein crystals. In the present study, we have carried out a systematic analysis of dichroism near the Se *K* edge in a selenated protein crystal. The absorption, refraction and resonant scattering tensors are derived from polarized fluorescence spectra. Some consequences of these findings for the design of beamline instrumentation, the optimization of data collection strategies and the improvement of phasing methods are discussed.

2. Materials and methods

2.1. Samples

The samples used in this study are crystals of recombinant selenomethionyl human aldose reductase complexed with its cofactor $NADP^+$ and with the inhibitor IDD594 ($C_{16}H_{12}NO_3BrF_2S$). These crystals belong to space group $P2_1$ with cell parameters a = 49.32, b = 66.90, c = 47.41 Å and β = 92.26°. The crystals diffract to very high resolution (better than 0.7 Å at undulator beamlines on third-generation synchrotrons) and the structure of the non-selenated molecule has been studied at the subatomic resolution of 0.66 Å (Podjarny *et al.*, 2004). The molecular weight of this monomeric enzyme is 35.8 kg mol^{-1} (kDa). It comprises 316 residues, of which six are selenomethionines. Thus, the content in Se atoms almost corresponds to the average expectation of one Se per 59 residues in selenated protein molecules (Hendrickson *et al.*, 1990). The selected molecule does therefore represent an ideal model system. There is one molecule in the asymmetric unit. There are thus 12 Se atoms in the unit cell. The inhibitor IDD594 contains a single Br atom that is covalently attached to a benzene ring. We have thus also qualitatively studied the AAS at the Br *K* edge. All data were collected on a single cryocooled (at 100 K) crystal of size 400 × 180 × 160 µm.

2.2. Polarized fluorescence measurements

All X-ray experiments were carried out at station BM01A of the Swiss–Norwegian Beamlines (SNBL) at the European Synchrotron Radiation Facility (ESRF) in Grenoble, France. This beamline is installed on a bending magnet and features a double Si(111) crystal monochromator. The endstation features a KM6-CH six-circle kappa diffractometer manufactured by Oxford Diffraction Ltd, and is equipped with a Tl:NaI scintillator point detector for the measurement of diffracted intensities. Previous measurements have established that the degree of linear polarization of the delivered X-ray beam is better than 0.96 (Birkedal, 2000). The experiments were carried out without focusing optics, thus producing a parallel beam with an energy bandwidth that is estimated to be ~1.9 eV at the Se *K* edge (see Appendix *A*). This energy resolution matches closely the bandwidth of monochromatic radiation that is commonly used on undulator-based macromolecular crystallography beamlines at third-generation synchrotrons, as is discussed in more detail in Appendix *A*. Our measurements were therefore carried out under experimental conditions of spectral purity and beam polarization which are representative of standard MAD experiments at third-generation synchrotrons.

An automatic peak-hunting procedure was used to find and measure a small number of Bragg reflections for the computation of an initial orientation matrix. Further reflections were then added and the final orientation matrix and cell parameters were refined on a set of 74 Bragg reflections. A complete set of data were measured in a small resolution shell at around 2.4 Å in order to assess the quality of the crystal: a merging R factor of 0.045 was obtained for 774 observations of 263 unique reflections. Polarized absorption spectra were measured in fluorescence mode with a Ce:YAP scintillation counter (Bede plc EDRc X-ray detector) mounted in the horizontal plane and perpendicular to the incident-beam direction in order to minimize the background contribution from elastic scattering processes. The wavelength was calibrated by recording the Pt L_{II} absorption edge (E = 13272.6 eV, λ = 0.9341 Å) on a platinum foil. For the recording of fluorescence spectra around the Se *K* edge (theoretical free-atom value: E = 12657.8 eV, λ = 0.9795 Å) the following layout was used: (i) energy range 12500–12630 eV: steps of 2 eV; (ii) energy range 12630–12640: steps of 1 eV; (iii) energy range 12640–12690: steps of 0.5 eV; (iv) energy range 12690–12700: steps of 1 eV; (v) energy range 12700–12900: steps of 2 eV. The counting time at each step was 5 s, which gave maximum counts of the order of 5×10^5. For the recording of fluorescence spectra around the Br *K* edge (theoretical free-atom value: E = 13473.7 eV, λ = 0.9202 Å) the following layout was used: (i) energy range 13400–13460 eV: steps of 2 eV; (ii) energy range 13460–13490: steps of 0.5 eV; (iii) energy range

13490–13520: steps of 1 eV; (iv) energy range 13520–13600: steps of 2 eV. The counting time at each step was 10 s, which gave maximum counts of the order of 10^6.

Fluorescence spectra at both the Se and Br *K* edges were recorded for six different crystal orientations. At one of the orientations, the polarization direction of the incident beam was aligned with the crystal **b** axis. For the five other orientations, the polarization direction was perpendicular to the crystal **b** axis at angles of respectively −42, −12, 18, 48 and 78° with respect to the crystal **a** axis. At each orientation and for each absorption edge, two consecutive spectra were recorded in order to check the reproducibility of the scans, which was excellent, *i.e.* the differences after scaling (see below) were within the error margins of counting statistics. The intensity of the incident beam was monitored by measuring the intensity scattered from a Kapton foil inserted in the direct beam path. The variation of the incident beam was observed to be smooth and virtually linear in each scan.

2.3. Data processing

For each scan, a linear fit was performed on the incident-beam monitor counts. These fits were then used to normalize the raw fluorescence data. Outlier points due to monochromator glitches were rejected manually. The two consecutive spectra recorded at each given orientation and for each absorption edge were merged for further processing. Background corrections, scaling of the experimental data to known theoretical values away from the edge, conversion of absorption coefficients to scattering factors and Kramers–Kronig transformations were carried out with the program *CHOOCH* (Evans & Pettifer, 2001).

Based on the atomic content of the unit cell (taking account of the solvent content), the linear absorption coefficients of the crystal at energies remote from the absorption edges were computed from tabulated values of f'' by using equations (1) and (2). The values μ = 254 and 394 m^{-1} were obtained for energies of respectively 12600 and 12800 eV. These value were used to put the experimental fluorescence data on an absolute scale.

For the decomposition of spectra onto principal directions a set of *ad hoc* computer programs written in Fortran 95 were used. All systems of linear equations were solved by singular-value decomposition.

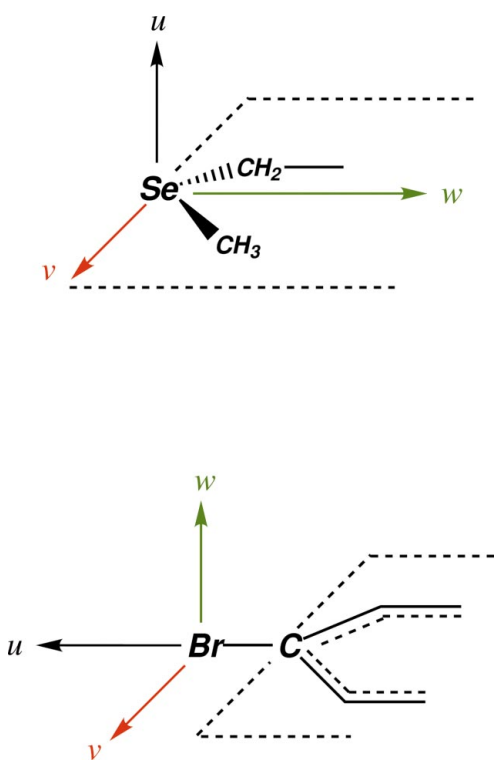

Figure 1
Molecular axes defining orthogonal principal directions at the level of the Se atoms in selenomethionine residues and at the level of the Br atoms in the inhibitor IDD594 (see §2.4).

Table 1
Direction of polarization.

For each of the six crystal orientations, the direction cosines of the polarization direction of the incident X-ray beam are expressed in crystal Cartesian coordinates referring to the orthonormal frame defined in §2.4.

Crystal orientation	*x*	*y*	*z*
1	−0.9512	0.0004	−0.3085
2	−0.0356	−0.9936	0.1068
3	−0.2091	0.0004	−0.9779
4	−0.7427	−0.0000	0.6696
5	−0.9780	0.0005	0.2085
6	−0.6698	0.0003	−0.7425

2.4. Cartesian coordinate frames for tensors

Crystal absorption, refraction and scattering tensors are expressed in an orthonormal basis (x, y, z) with axes x and z in the directions **a** and **c***, and y orthogonal to x and z. The direction of linear polarization of the incident X-ray beam is denoted by the unit vector **p**, which is always expressed in the orthonormal (x, y, z) basis. Components of the **p** vector are listed in Table 1 for each of the six crystal orientations. Thus, our frame of reference is the crystal, not the laboratory, and from this point of view, changing the crystal orientation actually amounts to a change in the direction of **p**.

Molecular axes defining orthogonal principal directions at the level of the Se atoms in selenomethionine residues are designated u for the direction perpendicular to the plane containing the C—Se—C bonds, w for the direction bisecting the C—Se—C angle and v for the direction perpendicular to u and w (see Fig. 1), corresponding respectively to the x, z and y directions defined by Templeton & Templeton (1988) in the selenolanthionine molecule.

Molecular axes defining orthogonal principal directions at the level of the Br atoms in the inhibitor IDD594 are designated u for the direction parallel to the C—Br bond, v for the direction perpendicular to the C—Br bond and parallel to the plane of the aromatic ring and w for the direction perpendicular to the aromatic ring (see Fig. 1), corresponding respec-

tively to the directions 1, 2, 3 defined by Templeton & Templeton (1995) in the molecule of homocubanecarboxylic acid *p*-bromoanilide.

3. Results and discussion

3.1. Polarized fluorescence spectra

Marked dichroism is observed in the polarized fluorescence spectra at the *K* edges of both Se and Br (see Figs. 2, 3 and 4). The fluorescence intensities at the Br *K* edge are somewhat noisier, due to the smaller number of Br atoms in the sample and also due to the fact that a strong fluorescence background from the Se atoms is still present at energies around the Br *K* edge. In what follows, we will therefore mainly focus on the analysis of the Se *K* edge data.

3.2. The absorption tensor: dichroism

We assume that the incident beam is linearly polarized along a crystal direction denoted $\mathbf{p}$. Then each spectrum k (*i.e.* each crystal orientation) samples a particular direction $\mathbf{p}_k$. The fluorescence intensity emitted at a given energy E from an infinitely small crystal is given by the quadratic form

$$I_k^{\rm fluo}(E) \propto \mu_k(E) = \mathbf{p}_k^{\rm T}\boldsymbol{\mu}(E)\mathbf{p}_k, \qquad (6)$$

where $\boldsymbol{\mu}$ denotes the absorption tensor, superscript T denotes transposition and μ_k denotes the effective scalar linear absorption coefficient along the direction $\mathbf{p}_k$.

In the general case, the reduction of fluorescence data into effective linear absorption coefficients μ_k is a highly non-trivial task for samples that are not infinitely small and that display dichroism and birefringence. The polarization vector of the incident beam can be decomposed along the principal directions of the crystal. Because of dichroism, each component will be absorbed differently. As a consequence, the polarization direction of the incident beam will be rotated as the beam propagates through the crystal. Birefringence will cause the components of the incident beam polarized along the different principal directions of the crystal to propagate at different velocities. Thus, as the beam propagates through the crystal, its polarization state will change from linear polarization to elliptical polarization. In the presence of dichroism and birefringence, different parts of the sample may therefore experience the incident beam under different polarization states, thus adding considerable complexity to the data analysis, although attempts have been reported in the literature (Lippmann *et al.*, 1996) to extract quantitative results from such measurements. The only situation where these complications are avoided is when the incident-beam polarization vector is aligned with one of the principal directions of the crystal. In the present case, however, the samples were sufficiently small and the resonant scattering sites were sufficiently diluted in the crystal that both dichroism and birefringence have only small effects on the polarization state of the incident beam as it propagates through the crystal. Model calculations presented in Appendix *B* show that for the crystal

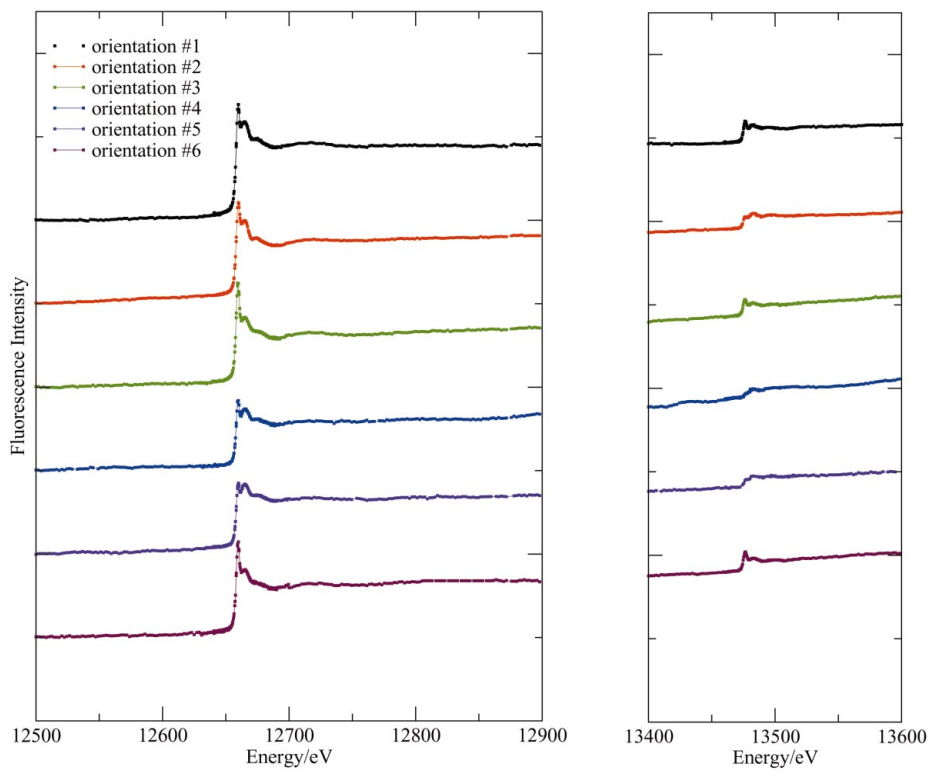

Figure 2
Polarized fluorescence spectra at the Se (left) and Br (right) *K* edges for each of the six crystal orientations. The plots represent the fluorescence intensity after normalization by the incident-beam intensity and by the counting time and after manual removal of outlier points which were due to monochromator glitches. Thus, all spectra are on the same scale, but they have been translated on the vertical axis for better visibility.

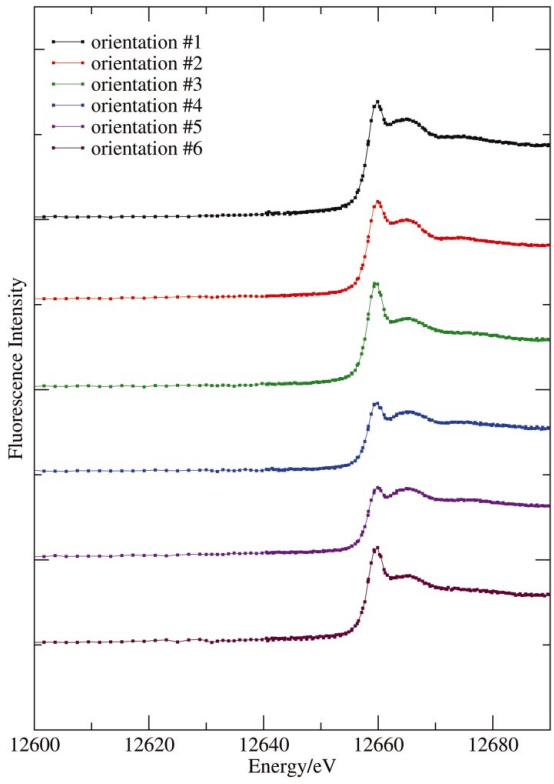

Figure 3
Polarized fluorescence spectra. Close-up view of the region around the Se K edge.

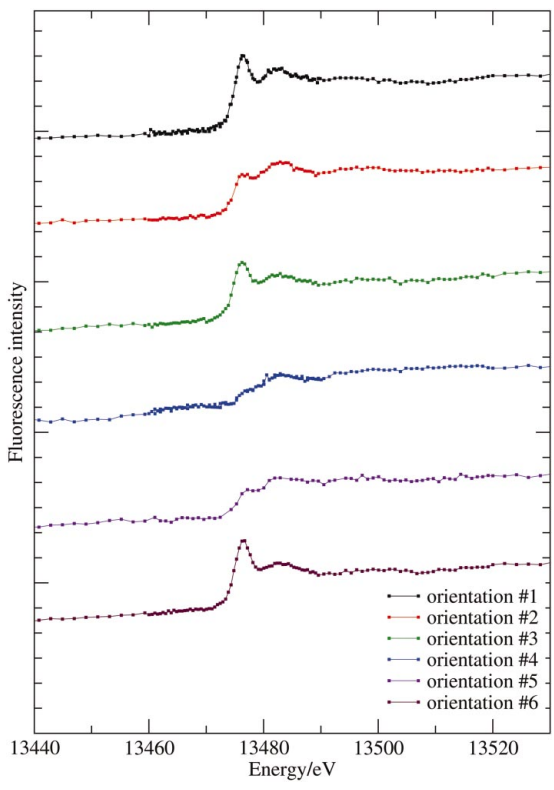

Figure 4
Polarized fluorescence spectra. Close-up view of the region around the Br K edge.

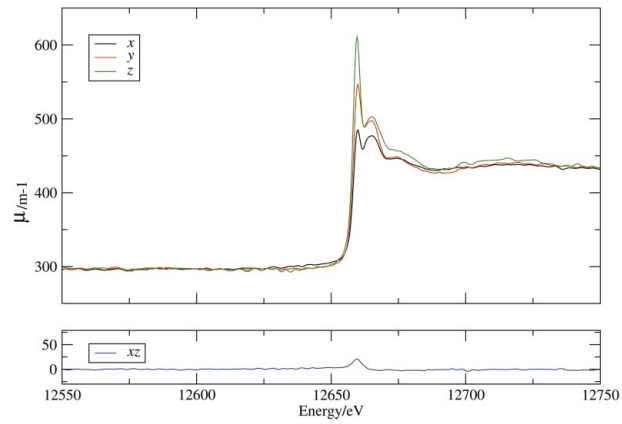

Figure 5
Absorption tensor $\boldsymbol{\mu}$ at the Se K edge. The plot represents the spectra of the four independent tensor elements μ_x, μ_y, μ_z and μ_{xz} as a function of X-ray energy at the Se K edge.

used in our experiments, the rotation of the polarization plane of the X-ray beam is less than 5°. Similarly, it is shown in Appendix C that birefringence has a negligible effect on the polarization state of the X-ray beam. Our data analysis was therefore conducted under the assumption that the polarization state of the incident X-ray beam is uniform throughout the sample. We further assumed that the incident beam is completely polarized in the horizontal plane (horizontal meaning here the plane defined by the orbit of the electron beam in the storage ring). Since the true degree of linear polarization of the beam is slightly less than 1, our results for crystal dichroism and AAS are slightly underestimated. Under these assumptions, the corrected fluorescence data $I_k^{\rm fluo}(E)$ can be converted to effective linear absorption coefficients $\mu_k(E)$ simply by scaling the data so that they agree with computed theoretical values at energies remote from absorption edges (Evans & Pettifer, 2001).

In the monoclinic crystal system with unique axis **b**, the point-group symmetry allows four independent elements for the absorption tensor

$$\boldsymbol{\mu}(E) = \begin{pmatrix} \mu_x(E) & 0 & \mu_{xz}(E) \\ 0 & \mu_y(E) & 0 \\ \mu_{xz}(E) & 0 & \mu_z(E) \end{pmatrix}. \qquad (7)$$

The six experimental spectra therefore form a system of linear equations in the unknown functions $\mu_x(E)$, $\mu_y(E)$, $\mu_z(E)$ and $\mu_{xz}(E)$:

$$\mu_k(E) = \mathbf{p}_k^{\rm T}\boldsymbol{\mu}(E)\mathbf{p}_k, \qquad k = 1, \ldots, 6. \qquad (8)$$

This system was solved by singular-value decomposition at each energy point E. The resulting spectra of tensorial elements are plotted in Figs. 5 and 6.

Probably more informative are the eigenvalues of the $\boldsymbol{\mu}$ tensor. These were computed individually at each energy step E and are plotted in Fig. 7. The difference between the largest and smallest eigenvalues corresponds to the maximum dichroism that can be observed in this crystal. As was noted in previous studies, dichroism is limited to a narrow region, of less than 100 eV width, in the immediate vicinity of absorption

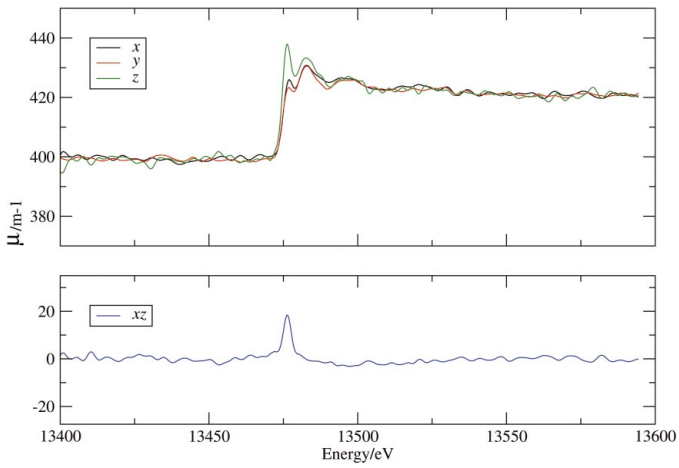

Figure 6
Absorption tensor $\boldsymbol{\mu}$ at the Br K edge. The plot represents the spectra of the four independent tensor elements μ_x, μ_y, μ_z and μ_{xz} as a function of X-ray energy at the Br K edge.

edges. The eigenvalues correspond to orthogonal eigenvectors. Because of the point-group symmetry constraints, one of the eigenvectors is parallel to the y direction (*i.e.* the crystal **b** axis). The orientation of the other two eigenvectors (which are contained in the xz plane) are observed to vary as a function of X-ray energy by as much as 15° in the near-edge region (12655–12663 eV), thus exhibiting orientational dispersion (Lippmann *et al.*, 1998).

3.3. The refraction tensor: birefringence

Since the real and imaginary parts of the complex index of refraction ($1 - \boldsymbol{\alpha}$ and $\boldsymbol{\beta}$) are related by the Kramers–Kronig transformation, the real correction part of the index of refraction could be computed from the $\boldsymbol{\mu}$ tensor:

$$\alpha_j(E) = \frac{2}{\pi}\mathcal{P}\int_0^\infty \frac{\beta_j(\mathcal{E})}{E^2 - \mathcal{E}^2}\mathcal{E}\,\mathrm{d}\mathcal{E}, \quad j = x, y, z, xz, \qquad (9)$$

where $\mathcal{P}$ denotes the Cauchy principal part of the integral and $\beta_j = (hc/4\pi E)\mu_j$. The eigenvalues of the $\boldsymbol{\alpha}$ tensor are plotted in Fig. 8 as a function of X-ray energy. At all energies, the difference between the smallest and largest eigenvalues is small relative to their mean values, thus indicating that birefringence is only a very minor effect in these crystals.

3.4. Principal values of the atomic resonant scattering tensors

In order to gain information about the AAS properties of the Se atoms in this crystal, we can postulate that the eigenvalues of the resonant scattering tensors are nearly identical for all Se atoms. This is a fairly reasonable assumption, since it amounts to recognizing that the immediate chemical environments are very similar for all Se atoms. The Se atoms in this crystal are all in selenomethionine residues in stable configurations. The side chain of one of the selenomethionine residues (SeMet-168) adopts two alternative conformations, which are well defined and have been refined against ultra-high resolution X-ray data. Thus, all Se sites are chemically equivalent in the sense that they have the same covalent binding environment and this is what is dominant for the resonant scattering factors in the near-edge region. Thus, we can assume that the resonant scattering tensors for all Se atoms have the same principal values. They are just oriented differently in space. Principal directions for the scattering tensors can be inferred from the local symmetry around the Se atoms as (i) the direction perpendicular to the plane containing the C—Se—C bonds, (ii) the direction bisecting the C—Se—C angle and (iii) the direction perpendicular to the first two (designated respectively by u, w and v). For each Se site, these directions are known from the ultra-high resolution crystal structure of the protein. For each Se site j in the crystal

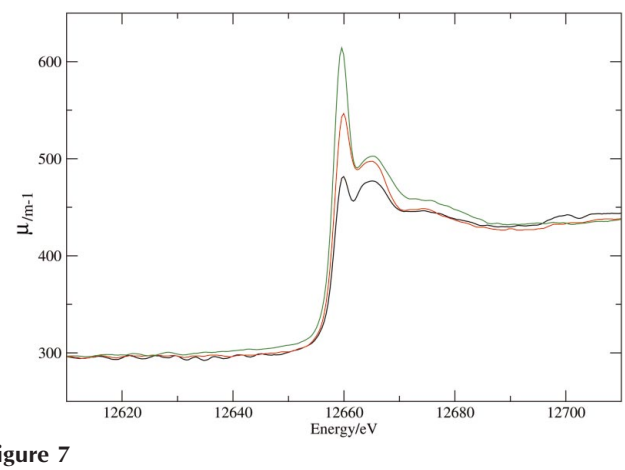

Figure 7
Eigenvalues of the absorption tensor at the Se K edge. The plot represents the spectra of the three eigenvalues of the $\boldsymbol{\mu}$ tensor as a function of X-ray energy at the Se K edge. The red curve represents the eigenvalues corresponding to the y direction (*i.e.* the crystal **b** axis). The other two curves represent eigenvalues corresponding to two mutually orthogonal directions in the xz plane which vary with X-ray energy [*i.e.* there is some orientational dispersion (Lippmann *et al.*, 1998) in this plane].

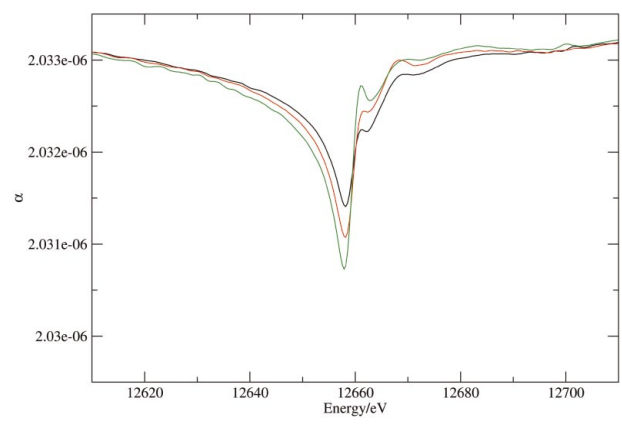

Figure 8
Eigenvalues of the refraction tensor at the Se K edge. The plot represents the spectra of the three eigenvalues of the $\boldsymbol{\alpha}$ tensor as a function of X-ray energy at the Se K edge. The red curve represents the eigenvalues corresponding to the y direction (*i.e.* the crystal **b** axis). The other two curves represent eigenvalues corresponding to two mutually orthogonal directions in the xz plane which vary with X-ray energy [*i.e.* there is some orientational dispersion (Lippmann *et al.*, 1998) in this plane].

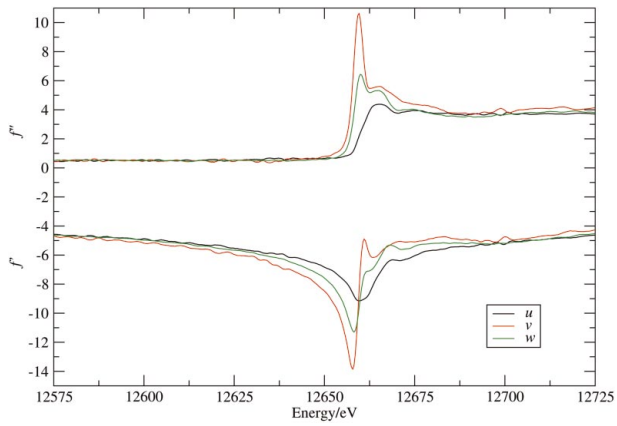

Figure 9
Principal values of the resonant scattering tensors for Se in selenomethionine residues. Black curves: along direction u (perpendicular to the plane containing the C—Se—C bonds). Green curves: along direction w (bisecting the C—Se—C angle). Red curves: along direction v (perpendicular to u and w).

unit cell, the resonant scattering tensors can thus be expressed by the following similarity transformations:

$$\mathbf{f}_j' = \mathbf{B}_j \boldsymbol{\Delta}' \mathbf{B}_j^{\mathrm{T}} \tag{10}$$

and

$$\mathbf{f}_j'' = \mathbf{B}_j \boldsymbol{\Delta}'' \mathbf{B}_j^{\mathrm{T}}, \tag{11}$$

where the $\mathbf{B}_j$ are orthogonal matrices whose columns are the vectors defining the principal directions u, v and w, and the matrices $\boldsymbol{\Delta}'$ and $\boldsymbol{\Delta}''$ are diagonal matrices whose elements are the principal values along the directions u, v and w:

$$\boldsymbol{\Delta}' = \begin{pmatrix} f_u' & 0 & 0 \\ 0 & f_v' & 0 \\ 0 & 0 & f_w' \end{pmatrix}$$

and

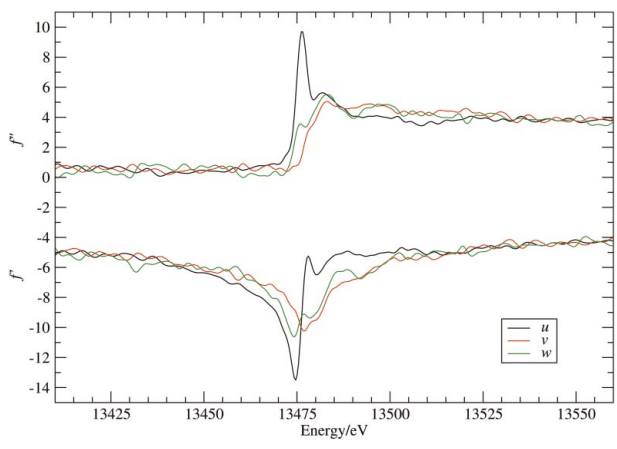

Figure 10
Principal values of the resonant scattering tensors for Br in the inhibitor IDD594. Black curves: along direction u (parallel to the C—Br bond). Red curves: along direction v (perpendicular to the C—Br bond and parallel to the plane of the aromatic ring). Green curves: along direction w (perpendicular to the aromatic ring).

$$\boldsymbol{\Delta}'' = \begin{pmatrix} f_u'' & 0 & 0 \\ 0 & f_v'' & 0 \\ 0 & 0 & f_w'' \end{pmatrix}. \tag{13}$$

Systems of linear equations can then be set up which relate the four independent elements of the refraction and absorption tensors $\boldsymbol{\alpha}(E)$ and $\boldsymbol{\mu}(E)$ to the unknown principal values $f_u'(E)$, $f_v'(E)$, $f_w'(E)$ and $f_u''(E)$, $f_v''(E)$, $f_w''(E)$:

$$\boldsymbol{\alpha}(E) = \alpha_{\mathrm{nr}}(E) + \frac{h^2c^2r_0}{2\pi VE^2} \sum_j^{N_{\mathrm{rs}}} Q_j \left[f_j^0(0) + \mathbf{B}_j \boldsymbol{\Delta}'(E) \mathbf{B}_j^{\mathrm{T}} \right] \tag{14}$$

and

$$\boldsymbol{\mu}(E) = \mu_{\mathrm{nr}}(E) + \frac{2hcr_0}{VE} \sum_j^{N_{\mathrm{rs}}} Q_j \mathbf{B}_j \boldsymbol{\Delta}''(E) \mathbf{B}_j^{\mathrm{T}}, \tag{15}$$

where the summations are over all N_{rs} resonant scattering atoms in the unit cell, *i.e.* $N_{\mathrm{rs}} = 14$ in the present case (owing to the fact that there are two molecules in the unit cell with six Se atoms per molecule, out of which one Se site has two alternative conformations) and Q_j is the occupancy factor of site j (which is equal to 1, except for the Se sites which have two alternative conformations). The terms $\mu_{\mathrm{nr}}(E)$ and $\alpha_{\mathrm{nr}}(E)$ denote respectively the absorption and refraction that is due to the non-resonant scattering atoms. Here, $\mu_{\mathrm{nr}}(E)$ and $\alpha_{\mathrm{nr}}(E)$ were computed from tabulated values of $f^0(0)$, $f'(E)$ and $f''(E)$, based on the atomic content of the unit cell. Both of these quantities show very little variation over the energy range under consideration.

These systems of linear equations were solved by singular-value decomposition at each energy point E and the resulting spectra of principal values are plotted in Fig. 9. The spectra of principal values obtained by this procedure are in very good agreement with values reported by Templeton & Templeton (1988) on selenolanthionine, namely that the white-line feature is most pronounced along the principal direction v, whereas it is virtually absent along the direction u. The maximum f_v'' value (10.6 at E = 12659.6 eV) is even higher than that reported for the selenolanthionine molecule.

A similar analysis was performed at the Br K edge and results are plotted in Fig. 10. As stated before, the data are somewhat noisier for the Br edge. Nevertheless the results are in good agreement with the data obtained previously for Br substituted on a benzene ring (Templeton & Templeton, 1995), namely that the white-line feature is most pronounced along the principal direction u (*i.e.* the direction parallel to the C—Br bond). It should also be noted that the decomposition into principal values is only meaningful in the immediate vicinity of the absorption edge, as the systems of linear equations [equations (15) and (14)] are degenerate at energies away from the edge, owing to the fact that $\mathbf{f}'$ and $\mathbf{f}''$ are in fact scalars at these energies. The oscillations that are observed in the spectra of the principal values below and above the edges are thus simply due to the noise in the data.

The atomic resonant scattering tensors $\mathbf{f}_j'$ and $\mathbf{f}_j''$ describe the AAS at the level of each individual selenium site j. The eigenvalue analysis of these tensors shows that very significant

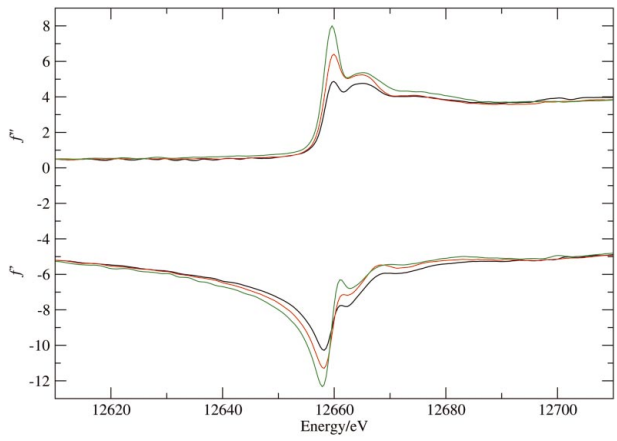

Figure 11
Eigenvalues of the average resonant scattering tensors at the Se K edge. The plot represents the spectra of the three eigenvalues of the $\bar{\mathbf{f}}''$ tensor (upper half) and the three eigenvalues of the $\bar{\mathbf{f}}'$ tensor (lower half) as a function of X-ray energy at the Se K edge. The red curves represent the eigenvalues corresponding to the y-axis direction (*i.e.* the crystal **b** axis). The black and green curves represent eigenvalues corresponding to two mutually orthogonal directions in the xz plane which vary with X-ray energy [*i.e.* there is some orientational dispersion (Lippmann *et al.*, 1998) in this plane].

modulations of scattering factors are possible as a function of the orientation of the C—Se—C group with respect to the direction of polarization of the incident beam. At the peak wavelength, variations of f'' values between 2.2 (for direction u) and 10.6 (for direction v) are possible. Similarly, at the first inflection point the f' values may vary between −8.6 (for direction u) and −13.8 (for direction v). At the second inflection point, the f' values vary between −4.9 (for direction v) and −9.0 (for direction u) as a function of crystal orientation. Interestingly, in going from one inflection point to the other, the difference $f'_u - f'_v$ changes sign. These values hold for scattering factors of individual Se atoms. Apart from the special case where all the C—Se—C groups are perfectly aligned in the crystal unit cell, different selenium sites will exhibit different resonant scattering factors at a given crystal orientation. Thus, symmetry-related selenium sites may not be equivalent anymore, as far as their scattering properties are concerned. As a consequence, point-group symmetry-related reflections may not be equivalent under such circumstances. For a rigorous treatment of diffraction data that are affected by AAS, it is therefore required (i) to keep the individual intensity measurements (*i.e.* no data merging), (ii) to keep track of the direction of polarization for each intensity measurement and (iii) to model the resonant scattering factors as tensorial quantities. This approach was pioneered by Fanchon & Hendrickson (1990), but has not been widely followed since then. If the data are merged and reduced to the asymmetric unit of the crystal point group (as is usually the case in macromolecular crystallography) the effective resonant scattering factor of a given symmetry-unique site is an average over the resonant scattering factors of all its symmetry-related sites.

3.5. Average resonant scattering tensors

The analysis of AAS in terms of atomic resonant scattering tensors is only possible if the orientations of all the C—Se—C groups in the crystal unit cell are known, *i.e.* once an electron density map of sufficient quality to indicate the C—Se—C planes is available. We can, however, define average resonant scattering tensors as

$$\bar{\mathbf{f}}' = \frac{1}{S_{\rm rs}} \sum_j^{N_{\rm rs}} Q_j \mathbf{f}'_j \qquad (16)$$

and

$$\bar{\mathbf{f}}'' = \frac{1}{S_{\rm rs}} \sum_j^{N_{\rm rs}} Q_j \mathbf{f}''_j \qquad (17)$$

where

$$S_{\rm rs} = \sum_j^{N_{\rm rs}} Q_j. \qquad (18)$$

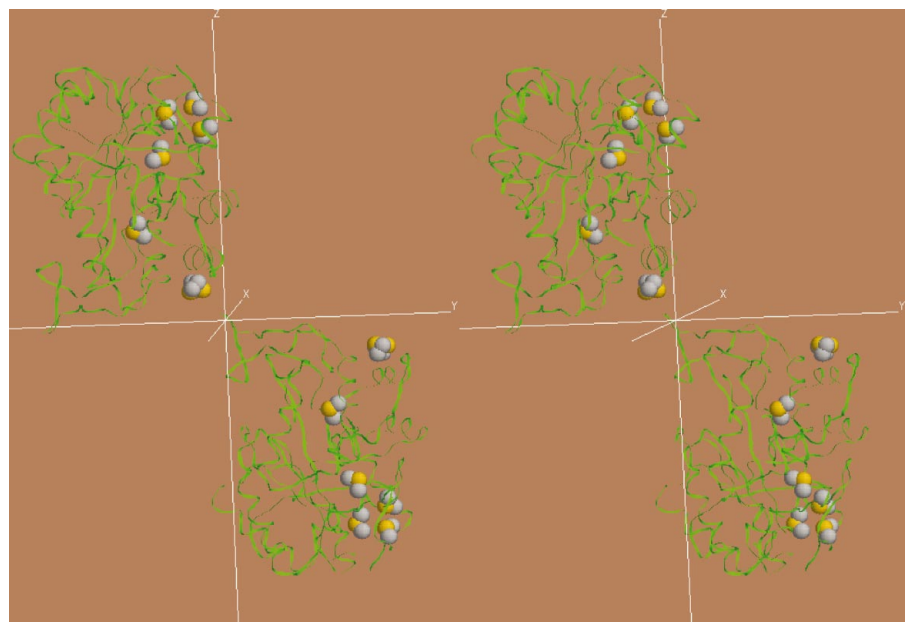

Figure 12
Stereoview representing all C—Se—C groups in the unit cell of crystals of selenated human aldose reductase. The Cα backbones of the two protein molecules are represented in green. Se atoms are represented in yellow and the Cγ and Cε atoms in selenomethionine side chains are represented in grey. Crystal axes (x, y, z) are also indicated. It can be seen from this representation that there is no obvious alignment of C—Se—C groups. The SeMet-168 residues (near the y axis) adopt two alternative conformations (see §3.4) which are represented as two very close C—Se—C moieties.

The $\bar{\mathbf{f}}'$ and $\bar{\mathbf{f}}''$ scattering tensors can be computed from the absorption and refraction tensors by using the optical theorem

$$\boldsymbol{\alpha}(E) = \alpha_{\rm nr}(E) + \frac{h^2c^2r_0}{2\pi VE^2}\, S_{\rm rs}\left[f^0_{\rm rs}(0) + \bar{\mathbf{f}}'(E)\right] \qquad (19)$$

and

$$\boldsymbol{\mu}(E) = \mu_{\rm nr}(E) + \frac{2hcr_0}{VE}\, S_{\rm rs}\bar{\mathbf{f}}''(E). \qquad (20)$$

Again, what is probably more informative are the eigenvalues of these average scattering tensors, denoted $\bar{f}'_1(E), \bar{f}'_2(E), \bar{f}'_3(E)$ and $\bar{f}''_1(E), \bar{f}''_2(E), \bar{f}''_3(E)$. These are plotted in Fig. 11. The data illustrate that large changes in average f' and f'' values are possible by varying the direction of polarization of the incident beam (*i.e.* by varying the crystal orientation). This point will be further discussed below.

Thus, the analysis of the macroscopic effects, dichroism and birefringence, can yield average resonant scattering tensors $\bar{\mathbf{f}}'$ and $\bar{\mathbf{f}}''$ without knowledge of the crystal structure. If the C—Se—C groups in the crystal unit cell are not perfectly aligned, the averaging of scattering tensors over all sites leads of course to some reduction of the overall anisotropy. This is demonstrated by comparing the principal values of the atomic resonant scattering tensors with the eigenvalues of the average resonant scattering tensors (compare Figs. 9 and 11). At *e.g.* the peak wavelength (E = 12659.6 eV), the reduction from f''_v = 10.6 to $(\bar{f}'')_{\rm max}$ = 8.0 is due to the averaging over C—Se—C groups that are oriented differently in the crystal unit cell.

It is important to realise that this averaging does not necessarily render the macroscopic effects and the average scattering isotropic. In other words, near-perfect alignment of C—Se—C groups in the crystal is not a prerequisite for the observation of dichroism. In the present case, there is no evident alignment of the C—Se—C groups in the unit cell (see Fig. 12), yet dichroism is clearly observable. The probability of a complete averaging to isotropy does of course increase as the number of sites in the unit cell increases, but the only cases where this is guaranteed to happen *a priori* are for cubic crystals. The probability of dichroism is particularly high for trigonal, tetragonal and hexagonal crystals since, for each resonant scatterer in the asymmetric unit, the AAS contribution along the unique axis is multiplied by the action of the three-, four- or sixfold symmetry operator.

3.6. Resonant scattering anisotropy *versus* oxidation of selenomethionine and their effects on fluorescence spectra

Our experiments demonstrate that AAS can give rise to large variations in the intensity of the white line at the Se K edge in polarized fluorescence spectra. However, oxidation of the selenium atoms also affects the near-edge features of fluorescence spectra, but it does so by shifting the energy position of the white line towards higher energies. This energy shift as a function of oxidation state is a well known fact in XANES spectroscopy and has been evidenced experimentally for several selenium-containing samples (Hunter *et al.*, 1997), including selenated proteins (Sharff *et al.*, 2000). On the other hand, AAS mainly affects the intensity of the white line and not its energy position.

In an analysis of fluorescence data from crystals of selenated *N*-myristoyl transferase, Smith & Thompson (1998) observed spectra which they qualified as 'aberrant' because of a greatly diminished white-line feature. They claim that the aberrant spectra cannot be due to AAS since this would only be observable when the C—Se—C planes in all selenomethionine residues in the sample are approximately parallel. This claim is not supported by our results. Clearly, to observe dichroism, it is not necessary that all C—Se—C groups be aligned. The spectrum which they qualify as 'aberrant' (Fig. 1*b* of Smith & Thompson, 1998) closely resembles the spectrum that we have recorded at orientation 5 in the present study (see Fig. 3). We therefore suggest that this spectrum has nothing 'aberrant', but that the diminished intensity of the white line is mainly a manifestation of AAS. Based on the principal values of the atomic resonant scattering tensors for Se in selenomethionine obtained from our data (see §3.4), we have simulated fluorescence spectra for crystals of selenated *N*-myristoyl transferase using the deposited coordinates of the structure. We find that these crystals should exhibit very significant dichroism: the white line is predicted to vary between 3.8 and 7.8 (smallest and largest eigenvalues of the computed $\bar{\mathbf{f}}''$ tensor at the peak energy) depending on whether the direction of polarization of the incident beam is aligned respectively with the crystal **c** or **b** axis. The 'aberrant' spectrum reported in Fig. 1*b* of Smith & Thompson (1998) does not display any energy shift of the white line as compared with a 'normal' spectrum (Fig. 1*a* of Smith & Thompson, 1998) collected at the same beamline under similar experimental conditions. Thus, the differences between these two spectra can be ascribed to AAS. These statements do not invalidate any of the conclusions drawn by Smith & Thompson (1998). We suggest, however, that great care should be exercised when interpreting and comparing fluorescence data recorded on randomly oriented crystals. We also suggest that the anomalous signal, especially at the white-line feature, can be optimized by choosing an appropriate crystal orientation.

4. Implications for data collection and processing strategies in macromolecular crystallography

4.1. Optimizing the anomalous phasing power by pre-orienting the crystal

4.1.1. General comments. For the vast majority of diffraction experiments in macromolecular crystallography, the screenless rotation method with an area detector and with a single scan axis is used. On most synchrotron beamlines, the scan axis is oriented parallel to the direction of linear polarization of the incident beam **p** (*i.e.* in the plane defined by the orbit of the electron beam and perpendicular to the incident X-ray beam direction). Thus, as the crystal is rotated during a data collection, the direction of polarization of the incident beam does not change with respect to the crystal. In other words, the vector **p** remains constant with respect to the crystal.

If the aim of the experiment is to maximize the anomalous phasing signal, the crystal should be pre-oriented in such a way that $\mathbf{p}$ is aligned with the crystal direction which corresponds to the largest eigenvalue of the $\bar{\mathbf{f}}''$ tensor. In the present case, a careful choice of crystal orientation would lead to an average f'' factor of 8.0 at the peak wavelength (see Fig. 11), whereas on a randomly oriented crystal smaller values (4.8, in the worst case) are obtained. An increase in average f'' factors from 4.8 to 8.0 is far from negligible and can give rise to a very significant improvement of the phasing power in SAD/MAD techniques. Fortunately, to determine the crystal direction along which the average f'' is maximum (*i.e.* the direction corresponding to the largest eigenvalue of the $\bar{\mathbf{f}}''$ tensor) it is not necessary to know the orientation of the individual selenomethionine side chains in the crystal. It is not even necessary to know the position of the Se atoms, since the $\bar{\mathbf{f}}''(E)$ tensors can be directly obtained from the macroscopic $\boldsymbol{\mu}(E)$ tensors. It is therefore enough to perform measurements of a small number of polarized fluorescence spectra at different crystal orientations and to reduce these to $\bar{\mathbf{f}}''(E)$ tensors. Diagonalization of the tensor at the peak energy will yield the crystal direction corresponding to its largest eigenvalue. It is then only required to align this direction with the scan axis (*i.e.* with $\mathbf{p}$). Obviously, the implementation of this procedure requires the use of a motorized and computer-controlled multi-axis goniometer for crystal orientation. We therefore advocate the systematic installation of such goniometers on synchrotron MAD beamlines.

For data recorded at the so-called inflection point (*i.e.* the energy corresponding to an extremum in the f' spectrum), it would in principle be necessary to carry out a separate analysis to diagonalize the $\bar{\mathbf{f}}'$ tensor and to align the crystal along the direction which corresponds to the largest absolute eigenvalue of this tensor. However, it turns out in practice that this direction is close to the one which optimizes the f'' signal.

4.1.2. Details of the procedure. We present here the practical procedure to determine the optimum crystal orientation in somewhat greater detail. It is required that an orientation matrix be available for the crystal under investigation. With modern autoindexing software it is usually possible to obtain a sufficiently accurate orientation matrix from just one or two diffraction frames, so that this step should be straightforward. It is further assumed that the crystal point group or at least the crystal system are known, as this information is anyway necessary to design the data collection strategy. The novel feature is the recording of several fluorescence spectra in definite crystal orientations, as opposed to the common practice of recording just one spectrum in a random crystal orientation. Each spectrum k samples a particular polarization direction $\mathbf{p}_k$ in the crystal. Each raw fluorescence spectrum is converted to an $f''(E)$ spectrum as described by Evans & Pettifer (2001). The set of $N_{\rm s}$ polarized spectra is then used to solve the system of linear equations

$$f_k''(E) = \mathbf{p}_k^{\rm T}\bar{\mathbf{f}}''(E)\mathbf{p}_k, \qquad k = 1, \ldots, N_{\rm s}, \tag{21}$$

for all tensorial elements of $\bar{\mathbf{f}}''(E)$ at each energy point E. Diagonalization of the tensor corresponding to the peak wavelength then yields the direction along which the average f'' is maximized.

Exactly how many and which spectra are to be recorded depends on the crystal system. A general constraint for the various directions $\mathbf{p}_k$ ($k = 1, \ldots, N_{\rm s}$) that are sampled is of course that they should all be non-equivalent under the Laue group symmetry of the crystal.

(i) For trigonal, tetragonal and hexagonal crystals, the point-group symmetry ensures that the $\bar{\mathbf{f}}''$ tensor is diagonal with only two independent elements.

$$\bar{\mathbf{f}}'' = \begin{pmatrix} \bar{f}''_{x|y} & 0 & 0 \\ 0 & \bar{f}''_{x|y} & 0 \\ 0 & 0 & \bar{f}''_{z} \end{pmatrix}. \tag{22}$$

It is therefore enough to record a minimum of two polarized fluorescence spectra ($N_{\rm s} \geq 2$) under the constraint that the two polarization directions ($\mathbf{p}_1$ and $\mathbf{p}_2$) must sample different absolute projections along the z axis (*i.e.* $|p_1^z| \neq |p_2^z|$). Ideally one would record a first spectrum with $\mathbf{p}$ perpendicular to z and a second one with $\mathbf{p}$ parallel to z. These would directly yield the $\bar{f}''_{x|y}$ and $\bar{f}''_z$ spectra. If other choices of orientations are made, the $\bar{f}''_{x|y}$ and $\bar{f}''_z$ spectra can be obtained by solving the appropriate system of linear equations. If, at the peak energy, $\bar{f}''_z > \bar{f}''_{x|y}$, the z axis should be aligned with the polarization direction. Otherwise, if $\bar{f}''_z < \bar{f}''_{x|y}$, any direction perpendicular to z is to be aligned with the polarization vector.

(ii) For orthorhombic crystals, the point-group symmetry ensures that the $\bar{\mathbf{f}}''$ tensor is diagonal with three independent elements.

$$\bar{\mathbf{f}}'' = \begin{pmatrix} \bar{f}''_{x} & 0 & 0 \\ 0 & \bar{f}''_{y} & 0 \\ 0 & 0 & \bar{f}''_{z} \end{pmatrix} \tag{23}$$

It is therefore enough to record a minimum of three polarized fluorescence spectra ($N_{\rm s} \geq 3$) under the constraint that the three $\mathbf{p}$ directions that are sampled must not be coplanar. Ideally one would record a first spectrum with $\mathbf{p}$ parallel to x, a second one with $\mathbf{p}$ parallel to y and the third one with $\mathbf{p}$ parallel to z. These would directly yield the $\bar{f}''_x$, $\bar{f}''_y$ and $\bar{f}''_z$ spectra. The crystal axis to be aligned with the polarization direction is the one which corresponds to the largest $\bar{f}''$ value.

(iii) For monoclinic crystals (unique axis $\mathbf{b}$), the point-group symmetry ensures that the $\bar{\mathbf{f}}''$ tensor has the following structure, with four independent elements

$$\bar{\mathbf{f}}'' = \begin{pmatrix} \bar{f}''_{x} & 0 & \bar{f}''_{xz} \\ 0 & \bar{f}''_{y} & 0 \\ \bar{f}''_{xz} & 0 & \bar{f}''_{z} \end{pmatrix}. \tag{24}$$

It is therefore necessary to record a minimum of four polarized fluorescence spectra ($N_{\rm s} \geq 4$) under the constraints that no more than three of the sampled $\mathbf{p}$ directions are coplanar and that the projections of these directions on the xz plane sample at least three different directions. Ideally one would record three spectra with $\mathbf{p}$ respectively parallel to x, y and z,

as well as a fourth spectrum with **p** parallel to the bisector of x and z. An eigenvalue/eigenvector analysis of the $\bar{\mathbf{f}}''$ tensor then yields the crystal direction which should be aligned with the polarization direction: it is the direction given by the eigenvector which corresponds to the largest eigenvalue.

(iv) For triclinic crystals, the $\bar{\mathbf{f}}''$ tensor has the general structure, with six independent elements

$$\bar{\mathbf{f}}'' = \begin{pmatrix} \bar{f}''_x & \bar{f}''_{xy} & \bar{f}''_{xz} \\ \bar{f}''_{xy} & \bar{f}''_y & \bar{f}''_{yz} \\ \bar{f}''_{xz} & \bar{f}''_{yz} & \bar{f}''_z \end{pmatrix}. \quad (25)$$

It is therefore necessary to record a minimum of six polarized fluorescence spectra ($N_s \geq 6$) under the constraint that no more than three of the sampled **p** directions are coplanar. Ideally one would record three spectra with **p** respectively parallel to x, y and z, as well as three spectra with **p** respectively parallel to each of the three bisectors of x, y and z. An eigenvalue/eigenvector analysis of the $\bar{\mathbf{f}}''$ tensor then yields the crystal direction which should be aligned with the polarization direction: it is the direction given by the eigenvector which corresponds to the largest eigenvalue.

The outlined algorithm can be easily be automated and integrated with the software that controls the diffractometer goniostat. The recording of fluorescence spectra is nowadays straightforward on virtually all MAD beamlines so that the additional time and effort spent in recording several spectra would be minimal.

4.2. Dichroism: implications for data reduction techniques

In macromolecular crystallography, absorption errors in the diffracted intensities are usually dealt with by empirical correction methods which exploit the redundancy of the data (Kabsch, 1988; Blessing, 1995). These methods aim at refining an empirical transmission surface by *e.g.* fitting a sum of spherical harmonic functions to maximize the consistency of the measured data. The arguments of the functions are direction vectors of the incident and scattered beams only. There is thus an implicit assumption in these methods that the absorption coefficient μ of the crystal is a scalar quantity. Our results show that this assumption may not be valid in the vicinity of an absorption edge. Especially for data recorded at the peak wavelength, pronounced dichroism may have a deleterious effect on the quality of the data, in particular for large crystals. Using our data for the absorption tensor $\boldsymbol{\mu}$, we can estimate that for a spherically shaped crystal (*i.e.* a crystal which has no shape anisotropy) with a diameter of 200 µm, the transmission of X-rays can vary by as much as 2.8%, depending on the orientation of the crystal with respect to the polarization direction of the X-ray beam. For a larger crystal with a diameter of 400 µm, the variations in X-ray transmission are estimated to be 5.5%. Such errors are not negligible and may harm the quality of the data, especially in MAD experiments where the phasing signal is obtained from small intensity differences. We therefore suggest that more sophisticated correction methods should be developed, where the empirical transmission surface would not only be a function of the incident- and scattered-beam directions, but also of the polarization directions of the incident and diffracted beams.

Part of this problem is, however, avoided (unintentionally!) by the current practice of recording data with a single scan axis which coincides with the direction of polarization of the incident beam (*i.e.* the direction **p** does not change during data collection). As a result, the absorption of the incident beam can be modelled as a single scalar quantity $\mu = \mathbf{p}^{\mathrm{T}}\boldsymbol{\mu}\mathbf{p}$ for all reflections. The effect of dichroism will thus be limited to the absorption of the scattered beams.

5. Conclusion

In this study we have presented a systematic analysis of X-ray dichroism, birefringence and AAS in a selenated protein crystal. These measurements were conducted under experimental conditions (beam polarization, spectral purity) which are representative of standard MAD experiments performed on third-generation synchrotrons. Significant dichroism and AAS were observed at energies close to the Se K edge. These effects are therefore likely to occur in many standard MAD experiments and they should be taken into consideration when designing the data collection strategy and at the data processing stage.

The effects of AAS can be handled and exploited at various levels of sophistication. The most involved method consists of refining the resonant scattering factors of individual atoms as tensorial quantities. This requires the use of unmerged data and the recording, for each intensity measurement, of the polarization properties of the incident X-ray beam and of the crystal orientation data (Fanchon & Hendrickson, 1990). The intensity differences in symmetry-related reflections can even yield additional phase information, which essentially comes for free. This might be of particular interest for breaking the phase ambiguity in single-wavelength anomalous diffraction (SAD) experiments. Another possibility would be to record data in several crystal orientations and to extract phase information from the observed intensity variations (Templeton & Templeton, 1991, 1992).

Even when data collection, processing and phase determination are carried out purely along conventional lines, the presence of AAS should be taken into account when planning the experiment, because a significant enhancement of the phasing signal is possible, simply by a judicious choice of crystal orientation. We have outlined a simple procedure of how this can be achieved, provided that an automated crystal goniostat is available. We therefore recommend that beamline scientists at synchrotrons systematically install or upgrade their diffractometers with such goniostats, particularly where SAD/MAD data are routinely collected.

APPENDIX *A*
Energy resolution of the incident radiation

We discuss here the energy bandwidth of the incident radiation used in our experiments and how this relates to the actual

bandwidth of commonly used macromolecular crystallography beamlines at third-generation synchrotrons, since the magnitude of the AAS effects depends critically on this parameter. The bandwidth is essentially determined by two factors: on the one hand, the intrinsic angular acceptance of the first monochromator crystal (the so-called Darwin width) $\omega_{\rm D}$ and, on the other hand, the angular spread $\psi_{\rm v}$ in the vertical plane of the fan of radiation that is intercepted by the optical elements of the beamline. Assuming Gaussian distribution functions, these two components can be convoluted to yield the relative energy resolution of the monochromated radiation as (Freund, 1993)

$$\Delta E/E = (\psi_{\rm v}^2 + \omega_{\rm D}^2)^{1/2}/\tan\theta, \qquad (26)$$

where θ is the monochromator Bragg angle. For a Si(111) monochromator, $\theta = 8.986^\circ$ at the Se K edge and $\theta = 8.438^\circ$ at the Br K edge. At energies close to the Se and Br K edges, the Darwin width of the Si(111) reflection is $\omega_{\rm D} \simeq 20$ µrad.

In our experiments, no focusing optics were used. Two pairs of slits mounted next to the sample were used to select a 0.5 × 0.5 mm portion of the incident beam. The maximum angular spread in the vertical plane of the fan of radiation that was directed towards the sample was therefore essentially determined by the aperture of the slits. The divergence which really counts is, of course, the fan of radiation intercepted by the crystal, but the aperture of the slits imposes a maximum value on this divergence. With the slits located at about 40 m from the source, we can estimate $\psi_{\rm v} \simeq 12$ µrad. Thus, the energy resolution at the Se K edge is estimated to be $\Delta E \simeq 1.9$ eV.

On undulator-based beamlines for macromolecular crystallography at third-generation synchrotrons, the divergence of the beam is usually so small that the full fan of radiation is used, without the need of a collimating pre-mirror. Thus, $\psi_{\rm v}$ is essentially identical to the vertical divergence of the beam which depends on the undulator parameters but is often of the order of 20 µrad (*e.g.* on SBC-19ID at the APS: $\psi_{\rm v}$ = 20–30 µrad; on PX at the SLS: $\psi_{\rm v}$ = 25 µrad). At the Se K edge this would give an energy spread of $\Delta E \simeq 2.2$ eV. If a collimating pre-mirror is used, the bandwidth will be smaller. A reduction of the bandwidth can also be achieved by using higher-order reflections such as Si(311) or Si(220), which is possible on some of the currently operated macromolecular crystallography beamlines.

We therefore claim that our experiments were conducted under conditions of spectral purity that closely match those of standard macromolecular diffraction experiments at third-generation synchrotrons.

APPENDIX *B*
Model computations on the effect of dichroism on the polarization state of the incident beam

In this and the following appendix, we evaluate the effect of dichroism and birefringence on the polarization state of an X-ray beam as it propagates through a selenated protein crystal at X-ray photon energies in the vicinity of the Se K absorption edge. To perform the model computations, we use the parameters of the crystal that was used in the present study. However, since the Se-atom content and the size of this crystal are representative for many selenated protein crystals that are used for diffraction studies, the conclusions that are drawn from these model computations are likely to hold beyond this particular sample.

We split the expression for the effective linear absorption coefficient μ into a non-resonant $\mu_{\rm nr}$ part and a resonant part $\mu_{\rm Se}$. Only the latter part, which is exclusively due to the Se atoms in the sample, creates dichroism.

$$\mu(E) = \mu_{\rm nr}(E) + \mu_{\rm Se}(E). \qquad (27)$$

The resonant part is due to the AAS of the Se atoms and is related to their $\mathbf{f}''$ scattering tensors.

$$\mu_{\rm Se}(E) = \mathbf{p}^{\rm T}\boldsymbol{\mu}_{\rm Se}(E)\mathbf{p} = \frac{2hcr_0}{VE}\sum_j^{\rm Se} Q_j\,\mathbf{p}^{\rm T}\mathbf{f}_j''(E)\mathbf{p}. \qquad (28)$$

The resonant part can assume maximum and minimum values that are related to the largest and smallest eigenvalues of the Se $\mathbf{f}''$ scattering tensors. We consider a worst-case scenario where all 12 C—Se—C substructures in the crystal unit cell are in the same orientation (with unit occupancies), thus giving rise to maximum dichroism. We further assume that the largest and smallest eigenvalues of the $\mathbf{f}''$ tensors are respectively $f''_{\rm max}$ = 10 and $f''_{\rm min}$ = 0. It should be noted that these values are respectively much higher and lower than those reported by Templeton & Templeton (1988) on selenolanthionine (7.7 and 0.8). The model computations presented here will therefore provide a safe upper limit for the effects of dichroism. At the Se K edge, the upper and lower bounds for the resonant part of the absorption coefficient are then evaluated as

$$(\mu_{\rm Se})_{\rm max} = (\mathbf{p}^{\rm T}\boldsymbol{\mu}_{\rm Se}\mathbf{p})_{\rm max} = \frac{2hcr_0}{VE}\,12 f''_{\rm max} = 423\,{\rm m}^{-1} \qquad (29)$$

and

$$(\mu_{\rm Se})_{\rm min} = (\mathbf{p}^{\rm T}\boldsymbol{\mu}_{\rm Se}\mathbf{p})_{\rm min} = \frac{2hcr_0}{VE}\,12 f''_{\rm min} = 0. \qquad (30)$$

We now consider the case where the polarization direction of the incident beam is at 45° with respect to the principal direction along which $\mu_{\rm Se}$ is maximum and also at 45° with respect to the principal direction along which $\mu_{\rm Se}$ is minimum (thus again representing a worst-case scenario). The incident beam can then be resolved into a component that is polarized along the first principal axis and whose intensity I_1 is attenuated as

$$I_1(d) \propto \exp\{-[\mu_{\rm nr} + (\mu_{\rm Se})_{\rm max}]\,d\} \qquad (31)$$

and an orthogonal component whose intensity I_2 is attenuated as

$$I_2(d) \propto \exp\{-[\mu_{\rm nr} + (\mu_{\rm Se})_{\rm min}]\,d\}, \qquad (32)$$

where d denotes the beam path length. The rotation of the polarization direction as the X-ray beam propagates through the crystal is then given by

$$\Theta(d) = \frac{\pi}{4} - \arctan\left[\frac{I_1(d)}{I_2(d)}\right] = \frac{\pi}{4} - \arctan[\exp(-\Delta\mu\, d)], \qquad (33)$$

where

$$\Delta\mu = (\mu_{\rm Se})_{\rm max} - (\mu_{\rm Se})_{\rm min} = 423\,{\rm m}^{-1}. \quad (34)$$

For d values of respectively 100, 200 and 400 µm, rotation angles of respectively 1.2, 2.4 and 4.8° are computed. Since the largest dimension of the crystal that was used in our experiments was 400 µm, the rotation of the polarization direction of the incident beam as it propagates through the crystal is at most 4.8°. In reality, the effect will be much smaller since the C—Se—C bonds of the 12 Se atoms in the crystal unit cell are not aligned. We can therefore assume to a good degree of approximation that dichroism has a negligible effect on the direction of polarization of the X-ray beam.

APPENDIX *C*
Model computations on the effect of birefringence on the polarization state of the incident beam

As before, we split the real part of the index of refraction $1 - \alpha$ into a non-resonant part $1 - \alpha_{\rm nr}$ and a resonant part $-\alpha_{\rm Se}$ that is due to the AAS of the Se atoms in the sample and is responsible for birefringence:

$$1 - \alpha(E) = 1 - \alpha_{\rm nr}(E) - \alpha_{\rm Se}(E). \quad (35)$$

The resonant part is related to the $\mathbf{f}'$ scattering tensors of the Se atoms:

$$\alpha_{\rm Se}(E) = \frac{h^2c^2r_0}{2\pi VE^2}\sum_j^{\rm Se} Q_j\,[f_j^0(0) + \mathbf{p}^{\rm T}\mathbf{f}_j'(E)\mathbf{p}]. \quad (36)$$

Again, we consider a worst-case scenario where all 12 Se atoms in the crystal unit cell are in the same orientation (with unit occupancies), thus giving rise to maximum birefringence. We also assume that the largest and smallest eigenvalues of the $\mathbf{f}'$ tensors are respectively $f'_{\rm max} = -5$ and $f'_{\rm min} = -15$. It should again be noted that these values are respectively much larger and smaller than those reported by Templeton & Templeton (1988) for selenolanthionine (−8.8 and −14.7). At the Se K edge, the upper and lower bounds for the resonant part of the index of refraction are then evaluated as

$$(\alpha_{\rm Se})_{\rm max} = \frac{h^2c^2r_0}{2\pi VE^2}\,12\,[f_{\rm Se}^0(0) + f'_{\rm max}] = 9.60\times10^{-9} \quad (37)$$

and

$$(\alpha_{\rm Se})_{\rm min} = \frac{h^2c^2r_0}{2\pi VE^2}\,12\,[f_{\rm Se}^0(0) + f'_{\rm min}] = 6.29\times10^{-9}. \quad (38)$$

We consider again the worst-case scenario where the polarization direction of the incident beam is at 45° with respect to the principal axis along which $\alpha_{\rm Se}$ is largest and also at 45° with respect to the principal axis along which $\alpha_{\rm Se}$ is smallest. The incident beam can then be resolved into a component that is polarized along the first principal axis and an orthogonal component which propagate at different velocities. If the incident beam is linearly polarized, these two components are initially in phase. As the X-ray beam propagates through the crystal, the two orthogonal components will acquire a phase difference that is given by

$$\Delta\varphi(d) = (2\pi/\lambda)\,\Delta\alpha\,d, \quad (39)$$

where d denotes the beam path length and

$$\Delta\alpha = (\alpha_{\rm Se})_{\rm max} - (\alpha_{\rm Se})_{\rm min} = 3.31\times10^{-9}. \quad (40)$$

For d values of respectively 100, 200 and 400 µm, phase differences of respectively 0.12, 0.24 and 0.49° are computed. Since the largest dimension of the crystal that was used in our experiments was 400 µm, the incident beam will remain almost linearly polarized as it propagates through the crystal (elliptical polarization would correspond to $\Delta\varphi = 90°$).

We are grateful to the members of the Global Phasing Consortium for financial support. We acknowledge partial financial support from European Commission Grant No. HPRI-CT-1999-50015 within the EXMAD project, and from Swiss National Science Foundation Grant No. 200021-101519. I. Hazemann and A. Podjarny are thanked for the gift of selenated aldose reductase crystals. G. Chapuis is thanked for his constant support of this project. We acknowledge the European Synchrotron Radiation Facility and the Swiss–Norwegian Beamline Consortium for provision of synchrotron radiation facilities and user beamtime.

References

Birkedal, H. (2000). *Use of Synchrotron Radiation in Chemical Crystallography*, PhD thesis, Université de Lausanne, Lausanne, Switzerland.
Blessing, R. H. (1995). *Acta Cryst.* A**51**, 33–38.
Dmitrienko, V. E. (1983). *Acta Cryst.* A**39**, 29–35.
Dmitrienko, V. E. (1984). *Acta Cryst.* A**40**, 89–95.
Evans, G. & Pettifer, R. F. (2001). *J. Appl. Cryst.* **34**, 82–86.
Fanchon, E. & Hendrickson, W. A. (1990). *Acta Cryst.* A**46**, 809–820.
Freund, A. (1993). *Neutron and Synchrotron Radiation for Condensed Matter Studies*, edited by J. Baruchel, J.-L. Hodeau, M. S. Lehmann, J.-R. Regnard & C. Schlenker, pp. 79–93. Berlin: Springer.
Hendrickson, W. A. (1991). *Science*, **254**, 51–58.
Hendrickson, W. A. (1999). *J. Synchrotron Rad.* **6**, 845–851.
Hendrickson, W. A., Horton, J. R. & LeMaster, D. M. (1990). *EMBO J.* **9**, 1665–1672.
Hendrickson, W. A., Pahler, A., Smith, J. L., Satow, Y., Merritt, E. A. & Phizackerley, R. P. (1989). *Proc. Natl Acad. Sci. USA*, **86**, 2190–2194.
Hodeau, J.-L., Favre-Nicolin, V., Bos, S., Renevier, H., Lorenzo, E. & Berar, J.-F. (2001). *Chem. Rev.* **101**, 1843–1867.
Hunter, D. B., Bertsch, P. M., Kemner, K. M. & Clark, S. B. (1997). *J. Phys. IV*, **7**(C2), 767–771.
Ishihara, S. & Maekawa, S. (2002). *Rep. Prog. Phys.* **65**, 561–598.
James, R. W. (1969). *The Optical Principles of the Diffraction of X-rays*. London: G. Bell.
Kabsch, W. (1988). *J. Appl. Cryst.* **21**, 916–924.
Kirfel, A. & Morgenroth, W. (1993). *Acta Cryst.* A**49**, 35–45.
Kirfel, A. & Petcov, A. (1992). *Acta Cryst.* A**48**, 247–259.
Kirfel, A., Petcov, A. & Eichhorn, K. (1991). *Acta Cryst.* A**47**, 180–195.
Lippmann, T., Fischer, K. & Kirfel, A. (1998). *J. Appl. Cryst.* **31**, 94–97.
Lippmann, T., Kirfel, A. & Fischer, K. (1996). *J. Appl. Cryst.* **29**, 186–197.
Ovchinnikova, E. N. & Dmitrienko, V. E. (2000). *Acta Cryst.* A**56**, 2–10.
Petcov, A., Kirfel, A. & Fischer, K. (1990). *Acta Cryst.* A**46**, 754–763.

Podjarny, A., Cachau, R. E., Schneider, T., Zandt, M. V. & Joachimiak, A. (2004). *Cell Mol. Life Sci.* **61**, 763–773.
Sharff, A. J., Koronakis, E., Luisi, B. & Koronakis, V. (2000). *Acta Cryst.* D**56**, 785–788.
Smith, J. L. & Thompson, A. (1998). *Structure*, **6**, 815–819.
Templeton, D. H. & Templeton, L. K. (1980). *Acta Cryst.* A**36**, 237–241.
Templeton, D. H. & Templeton, L. K. (1982). *Acta Cryst.* A**38**, 62–67.
Templeton, D. H. & Templeton, L. K. (1985*a*). *Acta Cryst.* A**41**, 133–142.
Templeton, D. H. & Templeton, L. K. (1985*b*). *Acta Cryst.* A**41**, 365–371.
Templeton, D. H. & Templeton, L. K. (1986). *Acta Cryst.* A**42**, 478–481.
Templeton, D. H. & Templeton, L. K. (1987). *Acta Cryst.* A**43**, 573–574.
Templeton, D. H. & Templeton, L. K. (1988). *Acta Cryst.* A**44**, 1045–1051.
Templeton, D. H. & Templeton, L. K. (1989). *Acta Cryst.* A**45**, 39–42.
Templeton, D. H. & Templeton, L. K. (1991). *Acta Cryst.* A**47**, 414–420.
Templeton, D. H. & Templeton, L. K. (1992). *Acta Cryst.* A**48**, 746–751.
Templeton, D. H. & Templeton, L. K. (1995). *J. Synchrotron Rad.* **2**, 31–35.
Templeton, D. H. & Templeton, L. K. (1997). *Acta Cryst.* A**53**, 352–355.